

Augmenting Landsat time series with Harmonized Landsat Sentinel-2 data products: Assessment of spectral correspondence

Michael A. Wulder^{a,*}, Txomin Hermosilla^a, Joanne C. White^a, Geordie Hobart^a,
Jeffrey G. Masek^b

^a Canadian Forest Service (Pacific Forestry Centre), Natural Resources Canada, 506 West Burnside Road, Victoria, British Columbia, V8Z 1M5, Canada

^b Biospheric Sciences Laboratory, NASA Goddard Space Flight Center, Greenbelt, MD, 20771, USA

ARTICLE INFO

Keywords:

Virtual constellation
Analysis ready data
Land cover
Monitoring
ARD
HLS

ABSTRACT

An increase in the temporal revisit of satellite data is often sought to increase the likelihood of obtaining cloud- and shadow-free observations as well as to improve mapping of rapidly- or seasonally-changing features. Currently, as a tandem, Landsat-7 Enhanced Thematic Mapper Plus (ETM+) and -8 Operational Land Imager (OLI) provide an acquisition opportunity on an 8-day revisit interval. Sentinel-2A and -2B MultiSpectral Instrument (MSI), with a wider swath, have a 5-day revisit interval at the equator. Due to robust pre- and post-launch cross-calibration, it has been possible for NASA to produce the Harmonized Landsat Sentinel-2 (HLS) data product from Landsat-8 OLI and Sentinel-2 MSI: L30 and S30, respectively. Knowledge of the agreement of HLS outputs (especially S30) with historic Landsat surface reflectance products will inform the ability to integrate historic time-series information with new and more frequent measures as delivered by HLS. In this research, we control for acquisition date and data source to cross-compare the HLS data (L30, S30) with established Landsat-8 OLI surface-reflectance measures as delivered by the USGS (hereafter BAP, Best Available Pixel). S30 and L30 were found to have high agreement ($R = 0.87\text{--}0.96$) for spectral channels and an $r = 0.99$ for Normalized Burn Ratio (NBR) with low relative root-mean-square difference values (1.7%–3.3%). Agreement between L30 and BAP was lower, with R values ranging from 0.85 to 0.92 for spectral channels and $R = 0.94$ for NBR. S30 and BAP had the lowest agreement, with R values ranging from 0.71 to 0.85 for spectral channels and $r = 0.90$ for NBR. Comparisons indicated a stronger agreement at latitudes above 55° N. Some dependency between spectral agreement and land cover was found, with stronger correspondence for non-vegetated cover types. The level of agreement between S30 and BAP reported herein would enable integration of HLS outputs with historic Landsat data. The resulting increased temporal frequency of data allows for improvements to current cloud screening practices and increases data density and the likelihood of temporal proximity to target date for pixel compositing approaches. Furthermore, additional within-year observations will enable change products with a higher temporal fidelity and allow for the incorporation of phenological trends into land cover classification algorithms.

1. Introduction

Earth observation satellites are a critical data source for the capture of both current status and dynamics in a wide range of environmental, economic, and scientific areas of interest (Hansen and Loveland, 2012; Townshend et al., 2012). Historically with fewer satellites in orbit, both mapping and monitoring activities were compromised by a number of issues, particularly a lack of data availability where and when data were desired (Belward and Skoien, 2015). The Landsat program has been

continuously collecting data since 1972, with notable advances in both technology and science integrated into the program and products over this 50-year period (Wulder et al., 2019). As exemplified by Landsat-8 Operational Land Imager (OLI), satellites now have greater capacity for storing data, disseminating them back to earth, and maintaining a precise position in orbit (Roy et al., 2014). Moreover, sensors have increasingly well-calibrated radiometry allowing for the conversion of observations to physical, science grade, surface reflectance values. High bandwidth downlink mitigated the need for global receiving networks,

* Corresponding author.

E-mail address: mike.wulder@nrcan-rncan.gc.ca (M.A. Wulder).

<https://doi.org/10.1016/j.srs.2021.100031>

Received 29 June 2021; Received in revised form 3 September 2021; Accepted 29 September 2021

Available online 1 October 2021

2666-0172/Crown Copyright © 2021 Published by Elsevier B.V. This is an open access article under the CC BY-NC-ND license

(<http://creativecommons.org/licenses/by-nc-nd/4.0/>).

reducing data latency as well as ensuring that all obtained data are centrally gathered and consistently processed. Free and open data policies (Woodcock et al., 2008; Wulder et al., 2012; Zhu et al., 2019) further allow agencies to ensure that once gathered and processed, data can be made analysis ready, thereby reducing pre-processing requirements for end users (Dwyer et al., 2018) and enabling greater consistency in analysis outcomes. The aforementioned is largely framed with an understanding of the Landsat program, but is increasingly applicable to Sentinel-2 (Drusch et al., 2012). Currently a tandem of satellites launched in 2015 and 2017, Sentinel-2A and -2B, respectively, both carry the Multi-Spectral Instrument (MSI), a sensor with complementarities with Landsat-8 OLI (in orbit since 2013; Roy et al., 2014). Pre- and post-launch calibration between Landsat-8 OLI and Sentinel-2 MSI (Helder et al., 2018) has resulted in a virtual constellation (Wulder et al., 2015), where the spectral band-passes generally align, further aided by high geometric agreement (Rengarajan et al., 2020). Since not all the spectral channels are of the same spatial resolution, a processing chain to harmonize the data from the two sources has been developed (Claverie et al., 2018). Key to the harmonization procedures are (i) creation of a common grid, pixel resolution, projection, and tiling system (spatial considerations); and (ii) application of a common radiative transfer algorithm to obtain complementary atmospherically corrected cloud masked surface reflectance data (spectral considerations). As a note, when we refer to spectral differences, we mean to include all sources of variability possibly influencing the spectral reflectance values, including uncorrected differences in spectral band-pass, differences in instrument calibration, or differences in angular response (e.g., Bidirectional Reflectance Distribution Function; BRDF).

As the amount, nature, and variety of analysis ready data (ARD) increases, users need to determine the applicability of a given dataset to their analysis and information needs, as well as the implications of combining different data sets. For instance, the United States Geological Survey (USGS) has been freely and openly distributing Landsat data since 2008 (Woodcock et al., 2008), including surface-reflectance data products. For the past decade, these data have formed the basis of numerous time series analyses undertaken over large areas (Hansen and Loveland, 2012; Wulder et al., 2019; Zhu, 2017). Given the previously noted limitations to acquisition frequency, it is only with Landsat-8 OLI that all potential terrestrial acquisitions have been obtained. Furthermore, the variability and small number of images that could be expected within a given year's growing season, limited the capacity and opportunities to inform algorithms. As such, many time-series projects were specified using limited within-year data, or used an annual time step. Following the launch of Sentinel-2 MSI and the virtual constellation with Landsat-8 OLI that resulted in the Harmonized Landsat Sentinel-2 (HLS) product, new opportunities now exist. Through the combination of Landsat-8 OLI and Sentinel-2A and -2B MSI, it is now possible to observe the global land surface every 2–4 days (depending on latitude) for a global median average revisit interval of 2.9 days (Li and Roy, 2017). Presence of a strong relationship between contemporaneous measures from the historic Landsat data stream and S30 (Sentinel-2 resampled to resemble 30-m Landsat) enables incorporation of the two data streams (archival USGS Landsat with HLS S30).

The objective of this research is therefore to determine the spectral correspondence between USGS and HLS sourced data. Spectral correspondence would enable combined use of both data sources in continued production of land cover (Hermosilla et al., 2018), forest change (Hermosilla et al., 2015a, 2015b), and forest structure products (Matsci et al., 2018a, 2018b) based upon annual image composites (e.g. Hermosilla et al., 2016) and enable refinement of science and applications approaches in an on-going fashion. In this research, we sample HLS and USGS sourced surface reflectance data across a massive spatial domain, stratify to ensure temporal agreement (i.e. same day of acquisition), and determine the strength and nature of cross-product spectral agreement.

2. Materials and methods

To determine the correspondence between USGS and HLS sourced data, we compared annual best-available-pixel (BAP) image composites produced using USGS Landsat data (Hermosilla et al., 2016) to HLS data products. All imagery was acquired during the growing seasons of 2015–2020. A random sample of HLS tiles was selected proportionally to the area of Canada's terrestrial ecozones. Spectral correspondence between observations was assessed by data sources (BAP, S30, and L30 which is the Landsat component from the HLS product) acquired on the same date, stratified by land cover and latitude.

2.1. Study area

The study area for this research is Canada (Fig. 1). Located in the northern hemisphere, Canada has highly seasonal weather, with marked differences between summer and winter temperatures and snow covered frozen ground common through winter months over much of its terrestrial area. With an area approaching 1 billion hectares, spanning thousands of kilometers both north-south and east-west, seasonal conditions and temperature vary by both latitude and longitude. Gradients in temperatures and seasonality result in differing dominant regional vegetation assemblages (Rowe, 1996). Moving north to south, snow-covered polar regions give way to ground vegetation and tundra ecosystems. Further south, terrestrial cover is a mix of ground vegetation and trees where local conditions allow, then forming a broad east-west band across Canada is the boreal forest. The boreal forest is characterised by trees (dominated by conifer species), wetlands, and lakes. South of the boreal are ecosystems with an increased presence of deciduous tree species found independently or in mixtures with conifers. Agricultural and industrial land uses are common in southern Canada, also where the majority of Canada's human population is found. As a means to ensure that the breadth and variety of land surface conditions present are captured in this study, ecozones (shown and labeled in Fig. 1) are used to guide a representative sampling approach described in Section 2.3.

2.2. Data

2.2.1. USGS sourced data (Best Available Pixel composites)

Image compositing enables the generation of wall-to-wall representation of a given area with similar conditions as well as the masking of cloud, shadow, and other atmospheric perturbations (Griffiths et al., 2013). We produced Best-Available-Pixel (BAP) composites for annual mapping and monitoring of Canada's forest-dominated ecosystems, capturing capture mid-summer vegetation conditions (Hermosilla et al., 2017). Following White et al. (2014) for this analysis, BAP composites were generated from Landsat-7 Enhanced Thematic Mapper Plus (ETM+) and Landsat-8 OLI images acquired from the USGS archive within the seasonal window of July 1st to August 31st each year between 2015 and 2020. The composites are comprised of six bands as indicated in Table 1. Landsat Collection 1 Level 1 data were downloaded via free and open access from the USGS. Surface reflectance is generated for all data using the LEDAPS algorithm (Masek et al., 2006; Schmidt et al., 2013). Cloud and shadow masks were generated with Fmask (Zhu and Woodcock, 2012). The rules used for selection of optimum pixels included comparing pixel scores generated based on temporal distance from August 1st (day of year, 213), spatial proximity to either cloudy or shadowed pixels, atmospheric opacity, and acquisition sensor (White et al., 2014). Such rules give priority to pixels acquired closer to the target date and penalize based upon atmospheric conditions and sensor.

2.2.2. Harmonized Landsat Sentinel-2 (HLS) data

The HLS initiative processes Landsat-8 OLI and Sentinel-2A and -2B MSI to create a spectrally-consistent product that is precisely geometrically co-registered with a 30-m spatial resolution. HLS undertakes to

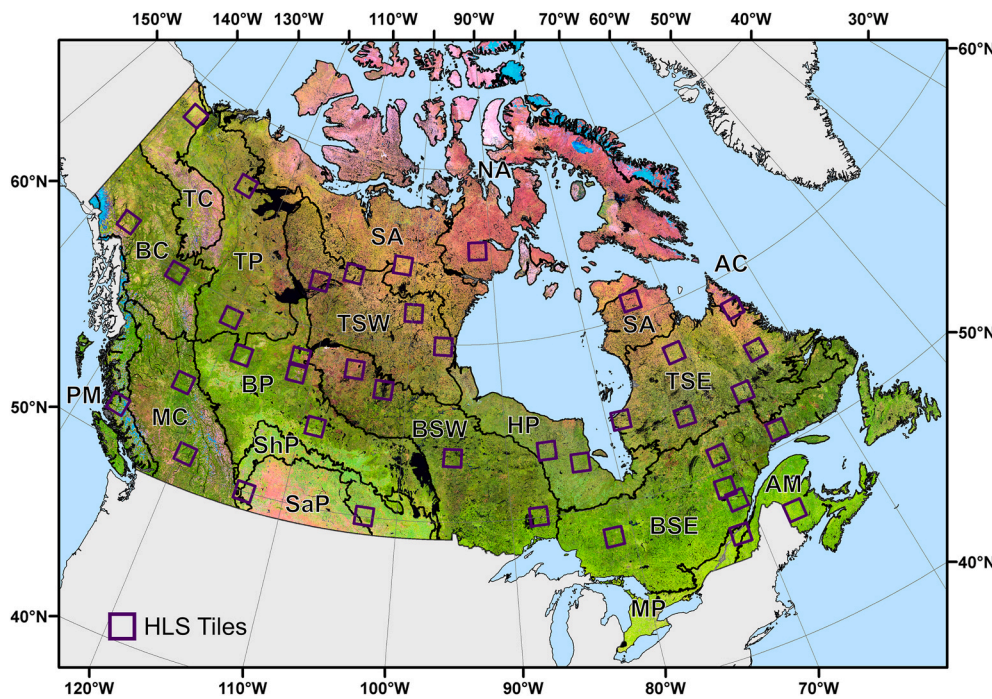


Fig. 1. Study area and location of the selected HLS tiles over Canada's ecozones. False color (bands: SWIR, NIR, R) Landsat image composite (Hermosilla et al., 2016). Ecozones: Arctic Cordillera (AC), Arctic Maritime (AM), Arctic Cordillera, Boreal Plains (BP), Boreal Shield East (BSE), Boreal Shield West (BSW), Hudson Plains (HP), Mixed-wood Plains (MP), Montane Cordillera (MC), Northern Arctic (NA), Pacific Maritime (PM), Semiarid Prairies (SaP), Southern Arctic (SA), Subhumid Prairies (ShP), Taiga Cordillera (TC), Taiga Plains (TP), Taiga Shield East (TSE), and Taiga Shield West (TSW). (For interpretation of the references to color in this figure legend, the reader is referred to the Web version of this article.)

Table 1
Harmonized Landsat Sentinel-2 nomenclature to link across OLI, MSI, and BAP data (after Masek et al. (2018)).

Band name	OLI band number	MSI band number	HLS band code name L8	HLS band code name S2	Common Basis (LC08)	BAP	Wavelength (micrometers)
Coastal Aerosol	1	1	band01	B01	B1		0.43–0.45*
Blue	2	2	band02	B02	B2	1	0.45–0.51*
Green	3	3	band03	B03	B3	2	0.53–0.59*
Red	4	4	band04	B04	B4	3	0.64–0.67*
Red-Edge 1	–	5	–	B05			0.69–0.71**
Red-Edge 2	–	6	–	B06			0.73–0.75**
Red-Edge 3	–	7	–	B07			0.77–0.79**
NIR Broad	–	8	–	B08			0.78–0.88**
NIR Narrow	5	8A	band05	B8A	B5	4	0.85–0.88*
SWIR 1	6	11	band06	B11	B6	5	1.57–1.65*
SWIR 2	7	12	band07	B12	B7	6	2.11–2.29*
Water vapor	–	9	–	B09			0.93–0.95**
Cirrus	9	10	band09	B10	B8		1.36–1.38*

Where: * from OLI specifications (may vary for S10 product which follow MSI specifications); ** from MSI specifications (Masek et al., 2018).

resolve differences in pixel size, spectral band-passes, as well as addressing data projection and tiling requirements (Claverie et al., 2018). In addition, due to swath width and differing orbital tracks (Roy et al., 2017), HLS products also have a Nadir BRDF Adjusted Reflectance (NBAR) correction applied (Claverie et al., 2018). The HLS data used in our analyses were taken from version 1.4 downloaded for the NASA HLS website (<https://hls.gsfc.nasa.gov/>) and included a Quality Assessment (QA) band, which indicates the presence of aerosols, water, snow/ice, clouds, and cloud shadows (Masek et al., 2018). Within a seasonal window (July 1st to August 31st) between 2015 and 2020, there was a total of 7656 HLS images available to download. Of these images there were 3440 S30 and 2047 L30 images meeting selection criteria, as described below.

As a note, the cirrus channel is used to improve screening of thin high-altitude cloud contamination through the detection of ice crystals that might not be visible at other optical band-passes (Qiu et al., 2020). In contrast to surface conditions, the atmospheric constituents detected at cirrus wavelengths (Table 1) are known to change rapidly, resulting in no expectation that cirrus be comparable between different sensors, even with short differences in observation time and date. As such, comparisons between cirrus channel data across sensors were not

reported.

2.2.3. Land cover

Land cover as an output of the Virtual Land Cover Engine (VLCE; Hermosilla et al. (2018)) representing 2018 conditions was used to aid with sample selection and for post-hoc analysis of spectral correspondence. VLCE is a Landsat-based image-classification approach that uses knowledge of disturbance and likelihood of transitions to inform the land cover mapping. VLCE uses a hierarchical classification legend comprising 12 land cover classes grouped in non-vegetated and vegetated. Non-vegetated classes included water, snow/ice (0.1% of the total sample units), rock/rubble (0.4%) and exposed/barren land (8.9%). Vegetated classes differentiate between non-treed and treed vegetation. Non-treed vegetation classes comprised bryoids (6.8%), herbs (23.8%), wetland (7.7%), and shrubs (6.7%). Treed vegetation classes included wetland-treed (6.3%), coniferous (20.4%), broadleaf (6.9%), and mixedwood (12%).

2.3. Sampling

A total of 40 Military Grid Reference System (MGRS) tiles were

randomly selected across Canada to align with the HLS scene delivery format. The tiles were selected on an area weighted basis by ecozone (Table 2). In so doing, we aimed to sample of all dominant ecosystems but also ensure the adequate representation of the largest ecosystems (Fig. 1). 20,000 random sample units (pixels) were generated for each selected MGRS tile. Both HLS and Landsat BAP datasets are in the Universal Transversal Mercator (UTM) projection. Clouds and shadows were masked out using the information provided by the QA information. A 3×3 -pixel analysis kernel was centred on the pixel centred on the pixel intersected by each sample point. To minimize differences due to spatial disagreement, the average of the 3×3 kernel was used to represent a given sample point. Thus we computed the mean value from every spectral band, as well as the Normalized Burn Ratio (NBR; Miller et al. (2009)) values. To ensure homogeneity of conditions only locations wherein all pixels within the analysis kernel had the same VLCE land cover class were selected. Day of year (DOY) and acquisition year is stored for each pixel to aid with further post-hoc analyses. Sample units from the BAP data source were only included when all pixels in the analysis kernel came from the same source Landsat-8 OLI image for all terrestrial land classes. Since L30 was obtained using Landsat-8 OLI, points including BAP pixels acquired from Landsat-7 ETM+ in a given analysis kernel were not considered in our analyses. This sampling criteria resulted in 3,451,108 sample units from L30, 5,172,639 from S30, and 1,499,154 from BAP. These samples were then used to assess spectral correspondence between the BAP, L30, and S30 data products.

2.4. Analysis

Spectral agreement by data source and channel (i.e. spectral band and NBR; Table 1) was analyzed using co-located sample units. BAP data were compared to HLS data differentiating between S30 and L30 data sources, and agreement between S30 and L30 was also analyzed as a benchmark comparison. For the pairwise observations (i.e., S30-L30, S30-BAP, and L30-BAP) only those pairwise observations with the same DOY and acquisition year were analyzed. Agreement between data sources was determined based on a suite of descriptive statistics, including Pearson correlation coefficient (r), mean difference as a

percentage of the range of the reference dataset (MD%), root-mean-square difference as a percentage of the range of the reference dataset (RMSD%), and the percentage of observations falling within ± 1 standard deviation ($\pm 1SD$) of the reference dataset.

$$MD = \frac{\sum (x_{ref} - x_{obs})}{n} \quad (1)$$

$$MD\% = \frac{MD}{range(x_{ref})} \times 100 \quad (2)$$

$$RMSD = \sqrt{\frac{\sum (x_{ref} - x_{obs})^2}{n}} \quad (3)$$

$$RMSD\% = \frac{RMSD}{range(x_{ref})} \times 100 \quad (4)$$

where x are the spectral values from each sample unit in the stratum, n is the number of sample units in that stratum (e.g., land cover, latitude), and range of the stratum. Herein we refer to the BAP as the primary reference dataset, as these data are the current source for derived information products (Hermosilla et al., 2016). In the case of L30 versus S30, L30 is considered the reference. The impact of land cover and latitude on spectral correspondence of NBR was assessed post-hoc. Land cover differentiated among non-vegetated and vegetated, and within the vegetated class among treed and non-treed (Hermosilla et al., 2018). The impact of latitude was assessed using 5° latitudinal ranges.

3. Results

Differences in acquisition DOY for the sample units, by data source, are shown in Fig. 2. From the total of pairwise observations that were acquired in the same day and year, S30-L30 comprised 495,155 (3.5%) observations, L30-BAP had 500,971 (15.4%) observations, and S30-BAP resulted in 136,787 (2.9%) observations. Note that the maximum value for S30-BAP corresponded to DOY = -1 (and as such these data were therefore not included in the sample). These data subsets were

Table 2

Distribution of samples by ecozone, MGRS tile, and area coverage. Summary of the number of sample units for each HLS and BAP data source.

Ecozone	Ecozone area (ha)	Number of MGRS tiles	MGRS tiles	Area covered by MGRS tiles (ha)	S30 sample units	L30 sample units	BAP sample units
Arctic Cordillera	24,158,168	1	20VMK	1,052,473	59,829	44,952	28,649
Atlantic Maritime	20,470,494	2	18TYS, 19TFM	1,550,399	206,324	119,155	50,613
Boreal Cordillera	44,471,984	2	08VMN, 09VWG	2,277,874	186,438	139,621	84,172
Boreal Plains	71,377,359	4	11VMD, 12UXF, 12VVJ, 12VVK	4,466,092	590,122	448,807	179,636
Boreal Shield East	107,771,042	7	17UMP, 18TYS, 18UYV, 19UCP, 19UCS, 19UFV, 19UGS	6,068,321	559,176	359,113	187,213
Boreal Shield West	81,820,987	6	12VVK, 13VDE, 13VFD, 14UQE, 16UDA, 16UEE	4,697,183	458,728	299,464	134,278
Hudson Plains	36,419,336	2	16UEE, 16UGD	2,342,008	341,323	233,174	95,065
Mixedwood Plains	17,393,448	1	18TYS	767,470	136,338	106,268	31,041
Montane Cordillera	47,786,279	4	09UXT, 10UEF, 10UGB, 11UQR	2,428,989	306,553	268,553	107,536
Northern Arctic	146,033,910	1	15WWN	1,134,349	188,832	120,278	37,108
Pacific Maritime	20,214,864	1	09UXT	1,130,793	30,506	47,698	42,237
Semiarid Prairies	23,868,137	2	11UQR, 13UFR	918,036	353,696	165,509	56,841
Southern Arctic	80,062,018	3	12VXR, 13WFM, 18VWN	2,373,871	175,263	114,639	39,480
Subhumid Prairies	22,148,100	2	11UQR, 13UFR	1,401,112	462,904	262,579	105,835
Taiga Cordillera	25,124,722	1	07WFR	1,138,327	111,707	97,059	33,506
Taiga Plains	61,994,274	3	09WXP, 10VFL, 11VMD	2,277,410	348,446	233,447	84,668
Taiga Shield East	73,088,636	6	17UPA, 18UXE, 19UFV, 19VCD, 20UMG, 20VMK	5,687,842	304,805	159,619	127,403
Taiga Shield West	59,806,811	6	12VVQ, 12VXR, 13VFD, 13WFM, 14VMP, 14VPM	4,446,589	351,649	231,173	73,873

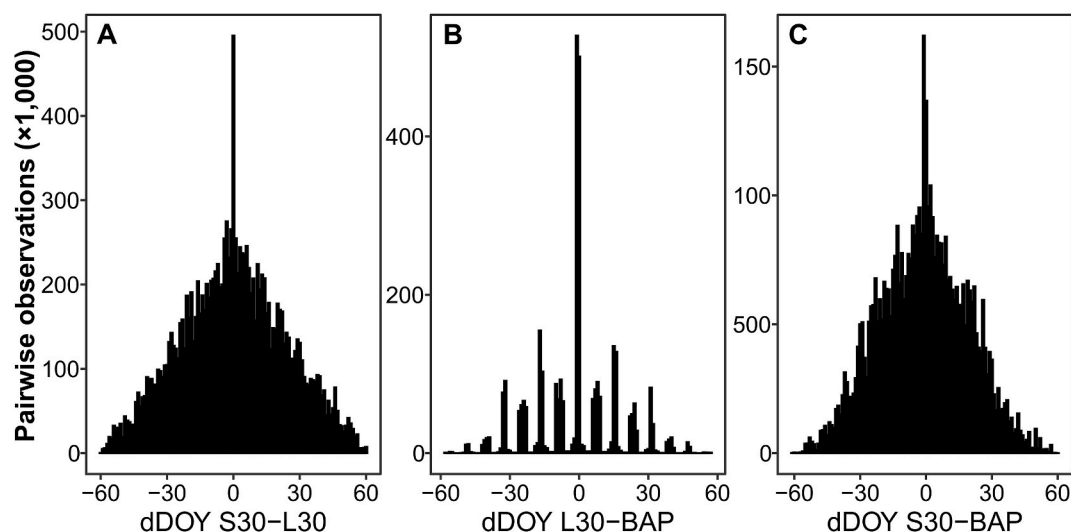


Fig. 2. Summary of distribution in differences in acquisition day of year (dDOY) for sample units by pairwise data sources: (A) S30-L30, (B) L30-BAP, and (C) S30-BAP. Note different y-axis values for interpretation and recall that only same year and same day (x-axis difference = 0) are used in further analyses.

subsequently used in our assessment of spectral agreement between the three data sources.

The correspondence between channels for the HLS data sources S30 and L30 is shown in Fig. 3A. As expected and given that S30 and L30 originate from the same data processing stream, the level of spectral correspondence between them was high. Correspondence (r) ranged from 0.87 to 0.96 for the spectral channels and $r = 0.99$ for NBR. RMSD % values were low, ranging from 1.7% to 3.3%. The lowest percentage of observations falling within ± 1 standard deviation was given for B1 (94.3%) and the highest for NBR (99.8%). MD% values were close to zero for all channels, with S30 surface reflectance values for B6 and B7 overestimated relative to the L30. Overall agreement between L30 and BAP (Fig. 3B) was slightly lower than between HLS data sources. Although both L30 and BAP data were acquired by Landsat, each is the product of different data processing streams. Correspondence (r) ranged from 0.85 to 0.92 for spectral channels and $r = 0.94$ for NBR. Relative to BAP, MD% indicated an overestimation of L30 surface reflectance for all channels but B2 and NBR. S30 and BAP presented the lowest agreement from the compared data sources (Fig. 3C), with r ranging from 0.71 to 0.85 for the channels and 0.9 for NBR. Of note, S30 surface reflectance values were found to be greater (1.3% on average) relative to BAP for all spectral channels and NBR in the context of the other comparisons (L30-BAP = 0.6% on average; L30-S30 = -0.2 on average).

Stratifying by VLCE land cover class, the spectral agreement for NBR between HLS data sources S30 and L30 was consistent for all land covers (Fig. 4A). Correspondence, however, varied by land cover when comparing between BAP and HLS data sources. Thus, spectral agreement for NBR was stronger for non-vegetated classes than for vegetated classes, as indicated by the greater r and ± 1 SD%, as well as smaller RMSD% values. Within the vegetated classes, the treed class had a higher level of correspondence in NBR values than non-treed. By data source, agreement between L30 and BAP (Fig. 4B) was consistently greater than between S30 and BAP (Fig. 4C). While L30 consistently underestimated NBR values relative to BAP, S30 was consistently found to have greater NBR values relative to BAP.

Table 3 shows the level of agreement in NBR between data sources by latitudinal range and land cover. Overall agreement between S30 and L30 was strong across the latitude gradient. RMSD% and ± 1 SD% indicated an increase in spectral correspondence with increasing latitude, with weaker agreement between data sources at lower latitudes, especially under 55° N. By land cover, non-vegetated class displayed the greatest variation in agreement by latitude. Note that these groups (non-vegetated and latitudes less than 55° N) also represent the smallest

sample populations and therefore these results should be interpreted with caution.

4. Discussion

Use of archival Landsat data augmented by new Landsat acquisitions has resulted in a myriad of science insights and operational information products. Besides open access, ARD is a key development spurring the increasing operational use of Earth observation data (Dwyer et al., 2018). Radiometric and geometric agreement over space and time is enabled by ARD, but typically only within a given sensor or sensor series. With the increasing availability of multispectral observations from differing optical sensors, information is required regarding the integrated use of these datasets. Following the launches of Sentinel-2A and -2B MSI in 2015 and 2017, respectively, to complement observations from Landsat-8 OLI (launched in 2013), a virtual constellation of complementary Earth observation data is now possible. The Harmonized Landsat Sentinel-2 product provides free and open access to Sentinel-2 MSI observations that are processed to enable interoperability with Landsat-8 OLI observations and thereby result in an enriched data stream.

At present, in order to meet national forest sector monitoring and reporting needs, Landsat time-series products are often designed to represent an annual time step. In many cases, this annual time step was determined based upon the availability of data in the USGS Landsat archive. On a scene basis, the number of images that can be expected differs over space and time (Goward et al., 2006; Wulder et al., 2016). Since the 1982 launch of Landsat-4 Thematic Mapper (TM), Landsat data products (TM, ETM+, OLI) have largely aimed to maintain comparable band-passes and spatial resolution, with robust cross-calibrations undertaken between Landsat sensors (Markham and Helder, 2012; Mishra et al., 2014). Since the launch of Landsat-8 OLI in 2013, the increase in on-board recording and higher bandwidth data downlink has meant that images are collected for all land on every overpass. Previous Landsat missions had limitations that required a more strategic acquisition approach, resulting in fewer images being obtained (Arvidson et al., 2001; Goward et al., 2006; Wulder et al., 2016) and available in the open access archive (Wulder et al., 2019). An annual time step implemented via best-available-pixel compositing is a means to obtain gap-free, consistent, spatial and temporal coverage over large areas. As such, there are effectively differing eras of possible product characteristics dictated by spatial and temporal data representation in the Landsat archive. When working in the Multispectral

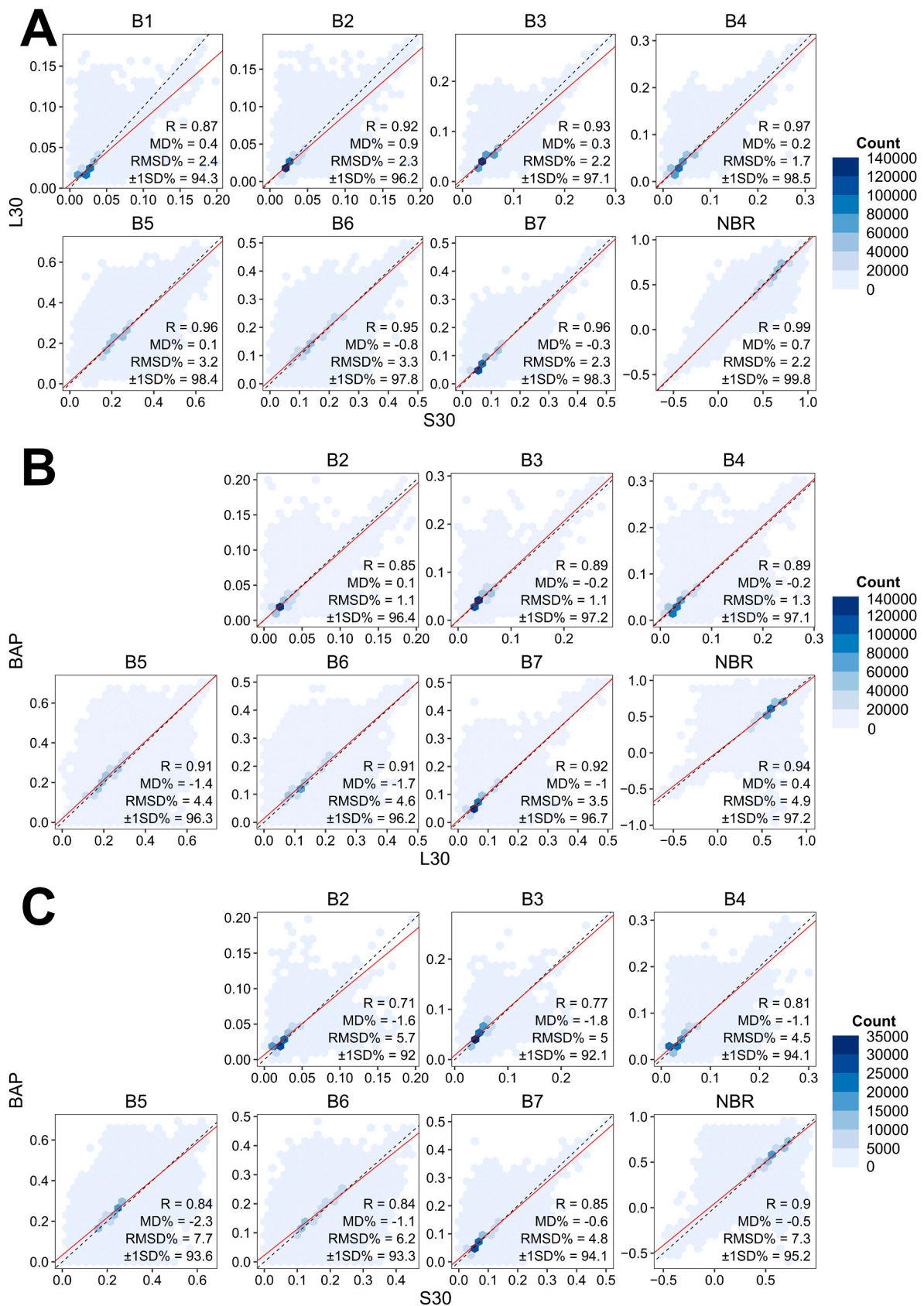


Fig. 3. Agreement by channel between (A) S30 and L30 data sources, (B) L30 and BAP data sources, and (C) S30 and BAP data sources. r = Pearson correlation coefficient, $MD\%$ relative mean difference, $RMSD\%$ = relative root mean square difference, $\pm 1SD\%$ = percentage of observations falling within ± 1 standard deviation. Note differing legends for the counts in each panel. The dashed line represents the 1:1 line, the red line represents linear best fit. (For interpretation of the references to color in this figure legend, the reader is referred to the Web version of this article.)

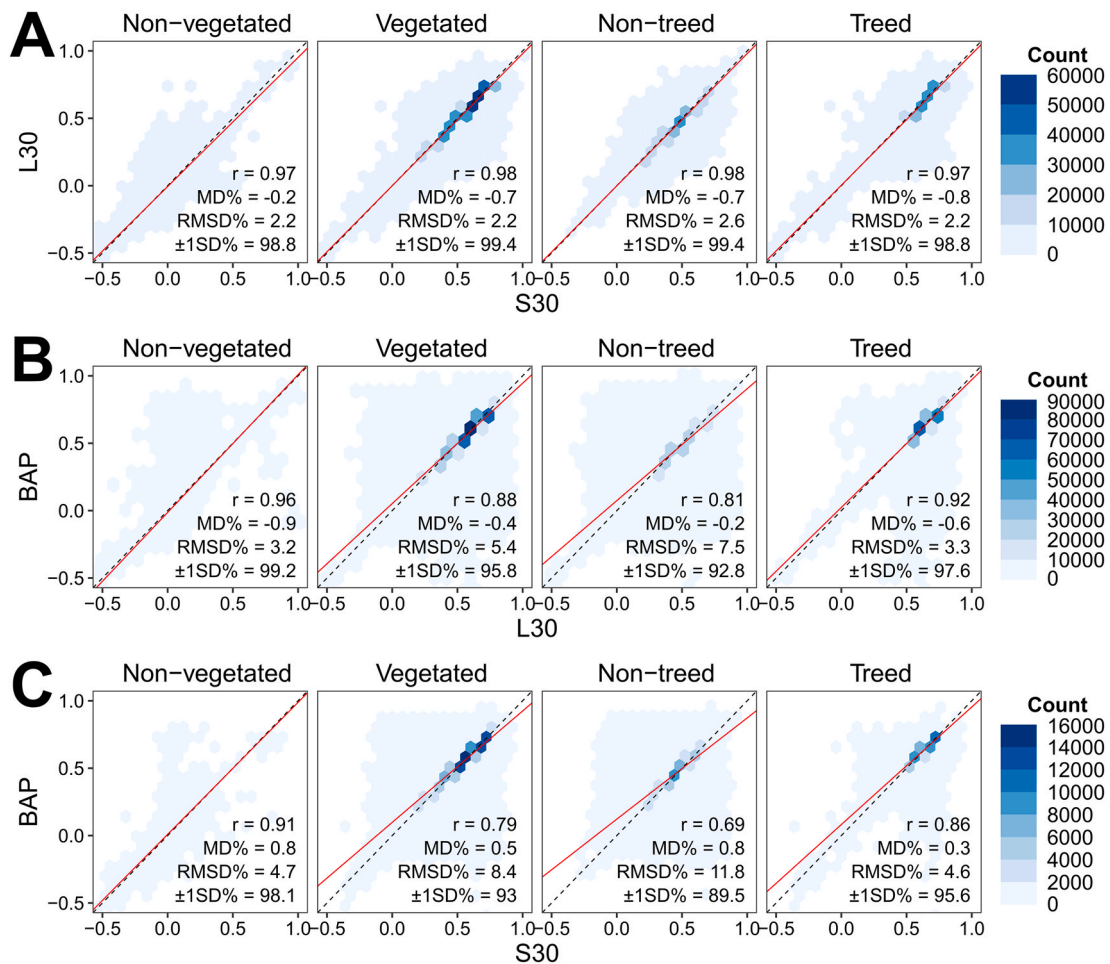


Fig. 4. Agreement of Normalized Burn Ratio (NBR) by land cover between (A) S30 and L30 data sources, (B) L30 and BAP data sources, and (C) S30 and BAP data sources. r = Pearson correlation coefficient, MD% = relative mean difference, RMSD% = relative root mean square difference, $\pm 1SD\%$ = percentage of observations falling within ± 1 standard deviation.

Scanner System (MSS) era (1972–1982), epochal products are required due to limited data availability. A baseline of 1975 is likely required to obtain sufficient images, even in locations where the MSS archival holdings are relatively rich when operating over larger areas. In the TM era (1982–1999), an annual time step is possible for many areas of the globe. With the 1999 launch of Landsat-7 ETM+ to complement Landsat-5 TM that was already in orbit, opportunities for generation of intra-year information were increased. These opportunities were further enhanced with the launch of Landsat-8 OLI in 2013, especially given the increased data yield over previous missions. It is this variability in expected image yield that has guided algorithmic decisions for derived information products, such as annually representative land cover and change mapping. With the launch in 2015 and 2017 of Sentinel-2A and -2B MSI in combination with Landsat-8 OLI, there is enhanced capacity for large area mapping and monitoring with an opportunity to have an observation for any location on a twice weekly basis.

Herein we explored the degree of spectral correspondence between BAP composites generated from archived USGS Landsat surface-reflectance data with HLS Landsat (L30) and Sentinel (S30) products. In examining a stratified sample of pixels representing a diverse geographic range of environmental gradients and land covers, we found strongest agreement between the L30 and S30 products, followed by the BAP and the L30, and the BAP and the S30. Overall, the level of spectral correspondence between the BAP and S30, particularly for the NBR ($r = 0.9$, MD% = 0.5), indicates that these data could be integrated in a virtual constellation to increase the density of observations for land. By land cover type the agreement between the BAP and S30 products was

stronger for non-vegetated ($r = 0.91$; $\pm 1SD\% = 98.1$) than vegetated classes ($r = 0.79$; $\pm 1SD\% = 93$). Within the vegetated land cover categories, correspondence was weaker for non-treed ($r = 0.69$; $\pm 1SD\% = 89.5$) than treed classes ($r = 0.86$; $\pm 1SD\% = 95.6$). The effect of the application of the NBAR correction (Claverie et al., 2018) to the HLS products is possibly manifest by the decrease in agreement between HLS and USGS Landsat products at lower latitudes. Overall correspondence between BAP and L30 was weaker ($r = 0.79$ to 0.81) for latitudes under than over 55° N ($r = 0.99$ to 1). Similarly for BAP and S30 agreement below 55° N ranged from $r = 0.69$ to 0.75 and between 0.95 and 0.98 above 55° N (Table 3). Landsat-8 acquires images with $\pm 7.5^\circ$ view angles from nadir. Differences in view angle can result in direction impacts upon observed surface reflectance, with greatest differences expected at lower latitudes (Nagol et al., 2015). HLS products include a BRDF correction to address the differences in view angles present between Landsat-8 and Sentinel-2 (view angles $\pm 10.3^\circ$). The adjustment is based upon the technique and coefficients provided by Roy et al. (2016) with the application outcomes further confirmed in Roy et al. (2017). The differences reported herein from our study between USGS surface reflectance and the surface reflectance values generated via the HLS processing stream are of the nature expected, with variability in differences found by land cover type and latitude.

Opportunities exist for applying models to gain further agreement between data from the differing OLI and MSI data streams (e.g., Chastain et al., 2019; Shang and Zhu, 2019). Data from sensors of the same satellite program are also known to differ spectrally over time (Markham and Helder, 2012) or as a function of operational considerations, such as

Table 3

Agreement of Normalized Burn Ratio (NBR) by latitude and land cover between S30 and L30, L30 and BAP and S30 and BAP data sources for NBR. r = Pearson correlation coefficient, MD% = relative mean difference, RMSD% = relative root mean square difference, $\pm 1SD$ % = percentage of observations falling within ± 1 standard deviation. Land cover classes: non-vegetated (NV), vegetated (V), vegetated non-treed (NT), and vegetated treed (T).

L30-S30																									
	r					RMSD%					MD%					±1SD%					Sample size				
Latitude	All	NV	V	NT	T	All	NV	V	NT	T	All	NV	V	NT	T	All	NV	V	NT	T	All	NV	V	NT	T
45-50	0.99	0.99	0.99	0.99	1.00	1.7	2.2	1.7	2.2	1.6	-0.6	-0.4	-0.6	-0.8	-0.6	99.9	99.4	99.9	99.9	98.5	124,277	471	123,806	68,384	55,422
50-55	0.98	0.99	0.98	0.99	0.90	2.2	2.3	2.3	2.6	2.5	-0.9	-0.3	-0.9	-1.0	-1.1	99.6	99.5	99.5	99.8	97.8	143,700	935	142,765	72,779	69,986
55-60	0.98	0.95	0.97	0.94	1.00	2.8	2.3	3.2	4.4	2.7	-0.7	0.0	-0.9	-0.7	-1.1	99.4	98.2	98.4	96.7	98.8	114,642	15,162	99,480	34,862	64,618
60-65	0.99	0.97	0.97	0.97	0.90	2.1	2.4	2.9	2.7	4.1	-0.6	-0.4	-0.9	-0.8	-1.1	99.8	99.1	98.9	98.8	98.1	68,165	15,257	52,908	43,865	9,043
65-70	0.99	0.96	0.95	0.95	0.90	2.6	3.1	3.4	3.3	6.5	-0.5	-0.5	-0.6	-0.6	-1.5	99.9	98.5	97.7	97.1	96.7	44,385	16,109	28,276	24,338	3,938

BAP-L30																									
	r					RMSD%					MD%					±1SD%					Sample size				
Latitude	All	NV	V	NT	T	All	NV	V	NT	T	All	NV	V	NT	T	All	NV	V	NT	T	All	NV	V	NT	T
45-50	0.79	0.40	0.79	0.72	0.77	8.9	27.6	9.1	12.7	6.3	-0.4	12	-0.4	0	-1.1	92.5	74	92.5	87.5	95.5	99,490	369	99,121	44,895	54,226
50-55	0.81	0.91	0.81	0.73	0.83	6.5	11.4	6.9	9.8	4.3	-0.4	2.9	-0.5	0	-0.8	94.5	92.7	94.4	90.9	95.8	186,565	1,226	185,339	72,444	112,895
55-60	0.99	0.99	0.97	0.93	0.98	2.5	1.8	2.9	4.4	2	-0.5	-1	-0.5	-0.4	-0.6	99.3	99.7	98.3	95.8	99.3	138,418	17,157	121,261	38,593	82,668
60-65	0.99	0.98	0.97	0.96	0.98	2.4	2.4	2.8	3	2.8	-0.7	-1.1	-0.7	-0.7	-0.9	99.7	99.6	99.2	99	99.3	46,437	9,185	37,252	28,815	8,437
65-70	1.00	0.98	0.96	0.95	0.94	2.7	3.4	3.2	3.5	5	-1.3	-2.4	-1.1	-1.2	-1.8	99.9	99.7	98.5	98.4	97.9	30,075	10,264	19,811	16,468	3,343

BAP-S30																									
	r					RMSD%					MD%					±1SD%					Sample size				
Latitude	All	NV	V	NT	T	All	NV	V	NT	T	All	NV	V	NT	T	All	NV	V	NT	T	All	NV	V	NT	T
45-50	0.75	0.27	0.74	0.65	0.75	11	26.4	10.9	14.7	6.2	10.3	1.4	0.7	1.4	-0.2	90.7	79.3	90.7	85.2	96.2	30,200	82	30,118	15,416	14,702
50-55	0.69	0.92	0.68	0.58	0.69	10	22.9	11.7	15.5	8.4	12	0.7	0.5	0.7	0.4	89.9	79.5	89.9	85.4	91.5	55,227	264	54,963	29,051	25,912
55-60	0.98	0.91	0.97	0.97	0.95	3.2	5.6	3.4	3.9	3.4	0.06	1	0.8	1	0.8	99.4	96.8	98.8	99	98.1	22,448	2,268	20,180	7,187	12,993
60-65	0.99	0.96	0.95	0.95	0.91	2.9	3.3	3.9	4	6	0.65	0.6	0.4	0.6	0.1	99.6	99.5	98.4	98.2	97.3	14,003	2,738	11,265	8,543	2,722
65-70	0.99	0.95	0.95	0.94	0.91	3	3.8	3.6	3.6	6.4	0.86	0.9	1	0.9	2.8	100	98.7	97.9	97.7	97.3	14,912	5,826	9,086	7,589	1,497

orbital drift (Zhang and Roy, 2016). Spectral agreement and thereby the potential for interoperability of disparate data streams, can be achieved via the application of a correction, whereby spectral agreement is assessed before and after a correction is applied and improvements are quantified (e.g. Chastain et al., 2019). Alternatively, spectral agreement may be improved by adjustments made in reference to expectations from other calibrated sensors (e.g., MODIS; Pustick et al., 2018). For instance, Roy et al. (2016) offer a general method and coefficients based upon MODIS data, to further process Landsat data to achieve an NBAR outcome globally. Future possible global ARD products are well positioned with supporting science to consider implementation of an NBAR adjustment. An acceptable level of spectral agreement can also be implicit through the delivery of ARD products. While the previous two aforementioned options alter data in order to engender improved spectral agreement; the provision of ARD products assumes that data are delivered in a useable form, especially when the data are already converted to physical values such as surface reflectance. In this research, we aimed to determine the capacity to treat Landsat and HLS outputs as complementary ARD products. The level of agreement for the unaltered spectral reflectance information from these two data streams was therefore of emphasis and interest in this research and found to agree for the northern latitudes dominated by Canada's forested ecosystems.

Since this study was performed, a new global version of HLS (v2.0) has been released. This version, available from the NASA Land Processes Distributed Active Archive Center (LP-DAAC) provides forward processing of L30 and S30 products from 2020 onward, with back processing of older (2013–2020) data to occur during 2022. While HLS v2.0 provides some enhancements including adjustments to the atmospheric correction and new product formats, the overall results from this study are not expected to be affected. The data from HLS v2.0 are not yet available for most of the years represented by this study (2015–2020).

5. Conclusions

In the field of Earth observation, a number of advances in both space- and ground-based data management systems have occurred in recent years. Space agencies have cooperated in meaningful ways to ensure spectral alignment for recent sensor developments and subsequent launches, as exemplified by the OLI on Landsat-8 and the MSI on the Sentinel-2 satellites, effectively demonstrating a virtual constellation. Ground systems that avail upon data streams of calibrated data to produce physical values (surface reflectance) as ARD products allow for use of the data in an integrated form and as inputs to further spatial and spectral processing for a harmonized multi-sensor product. As physical values, surface reflectance provides a bridge across sensors, as well as with historic data acquisitions. Time series analysis benefits from the use of non-normalized data (to avoid smoothing), making the direct use of surface reflectance from differing data streams desirable. Across a massive spatial domain, our results indicate strong agreement ($r = 0.95$ to 0.96) for non-visible spectral bands, which are less influenced by atmospheric effects, from the Sentinel-2 MSI (S30) and Landsat-8 OLI (L30) outputs derived from the HLS processing stream. Likewise, strong agreement was indicated between these HLS products and non-HLS surface reflectance products for the NIR and SWIR channels ($r = 0.84$ to 0.85). Agreement varied latitudinally as a result of the application of the NBAR correction over the HLS data sources. Stronger correspondence was found for latitudes above 55° N ($r = 0.95$ to 0.96 , RMSD% = 2.5 to 2.7) than below ($r = 0.79$ to 0.81 , RMSD% = 6.5 to 8.9) demonstrating application utility in the context of Canada's forested ecosystems. The ability to operationally incorporate HLS data into data processing streams that were previously Landsat-only is supported by these results, thereby expanding available observations for the production of cloud- and gap-free pixel composites focused on a particular

target date, as well as increasing capacity to capture within-year spectral information (e.g. green-up, phenology, leaf-on/off) for improving land cover and change mapping. Of note, correspondence between S30 and L30 data sources was the strongest, demonstrating the internal consistency of HLS products. As such, HLS products are well suited as a contemporary data stream integrating Sentinel-2 MSI and Landsat-8 OLI, since L30 and S30 are both subject to an NBAR correction. For analysis involving historic (pre-HLS) data, there is strong agreement with USGS-derived Landsat-8 OLI surface reflectance values and vegetation indices, as demonstrated herein, with only slight differences present that are related to the differing nature of the processing applied.

Declaration of competing interest

The authors declare that they have no known competing financial interests or personal relationships that could have appeared to influence the work reported in this paper.

Acknowledgements

The authors thank and appreciate the efforts of the journal editors in expertly handling this manuscript and the reviewers that offered collegial and helpful insights and suggestions. The leadership and vision of John Dwyer in making analysis ready data a core element of USGS programs and products is acknowledged and lauded. Harmonized Landsat Sentinel-2 v1.4 data can be found following: <https://hls.gsfc.nasa.gov/>, and v2.0 at: <https://www.usgs.gov/core-science-systems/nli/landsat/landsat-data-access>.

References

- Arvidson, T., Gasch, J., Goward, S.N., 2001. Landsat 7's long-term acquisition plan - an innovative approach to building a global imagery archive. *Remote Sens. Environ.* 78, 13–26. [https://doi.org/10.1016/S0034-4257\(01\)00263-2](https://doi.org/10.1016/S0034-4257(01)00263-2).
- Belward, A.S., Sköien, J.O., 2015. Who launched what, when and why; trends in global land-cover observation capacity from civilian earth observation satellites. *ISPRS J. Photogrammetry Remote Sens.* 103, 115–128. <https://doi.org/10.1016/j.isprsjprs.2014.03.009>.
- Chastain, R., Housman, L., Goldstein, J., Finco, M., 2019. Empirical cross sensor comparison of Sentinel-2A and 2B MSI, Landsat-8 OLI, and Landsat-7 ETM+ top of atmosphere spectral characteristics over the conterminous United States. *Remote Sens. Environ.* 221, 274–285. <https://doi.org/10.1016/j.rse.2018.11.012>.
- Claverie, M., Ju, J., Masek, J.G., Dungan, J.L., Vermote, E.F., Roger, J.C., Skakun, S.V., Justice, C., 2018. The Harmonized Landsat and Sentinel-2 surface reflectance data set. *Remote Sens. Environ.* 219, 145–161. <https://doi.org/10.1016/j.rse.2018.09.002>.
- Drusch, M., Del Bello, U., Carlier, S., Colin, O., Fernandez, V., Gascon, F., Hoersch, B., Isola, C., Laberinti, P., Martimort, P., Meygret, A., Spoto, F., Sy, O., Marchese, F., Bargellini, P., 2012. Sentinel-2: ESA's optical high-resolution mission for GMES operational services. *Remote Sens. Environ.* 120, 25–36. <https://doi.org/10.1016/j.rse.2011.11.026>.
- Dwyer, J.L., Roy, D.P., Sauer, B., Jenkerson, C.B., Zhang, H.K., Lymburner, L., 2018. Analysis ready data: enabling analysis of the landsat archive. *Rem. Sens.* 10, 19–Jan. <https://doi.org/10.3390/rs10091363>.
- Goward, S., Arvidson, T., Williams, D., Faundeen, J., Irons, J., Franks, S., 2006. Historical record of landsat global coverage: mission operations, NSLRSDA, and international cooperator stations. *Photogramm. Eng. Rem. Sens.* 72, 1155–1169.
- Griffiths, P., van der Linden, S., Kuemmerle, T., Hostert, P., 2013. A pixel-based landsat compositing algorithm for large area land cover mapping. *IEEE J. Sel. Top. Appl. Earth Obs. Remote Sens.* 6, 2088–2101. <https://doi.org/10.1109/jstars.2012.2228167>.
- Hansen, M.C., Loveland, T.R., 2012. A review of large area monitoring of land cover change using Landsat data. *Remote Sens. Environ.* 122, 66–74. <https://doi.org/10.1016/j.rse.2011.08.024>.
- Helder, D., Markham, B., Morfitt, R., Storey, J., Barsi, J., Gascon, F., Clerc, S., LaFrance, B., Masek, J., Roy, D., Lewis, A., Pahlevan, N., 2018. Observations and recommendations for the calibration of landsat 8 OLI and Sentinel 2 MSI for improved data interoperability. *Rem. Sens.* 10, 1340. <https://doi.org/10.3390/rs10091340>.
- Hermosilla, T., Wulder, M.A., White, J.C., Coops, N.C., Hobart, G.W., 2018. Disturbance-informed annual land cover classification maps of Canada's forested ecosystems for a 29-year landsat time series. *Can. J. Rem. Sens.* 44, 67–87. <https://doi.org/10.1080/07038992.2018.1437719>.
- Hermosilla, T., Wulder, M.A., White, J.C., Coops, N.C., Hobart, G.W., 2017. Updating Landsat time series of surface-reflectance composites and forest change products with new observations. *Int. J. Appl. Earth Obs. Geoinf.* 63, 104–111. <https://doi.org/10.1016/j.jag.2017.07.013>.
- Hermosilla, T., Wulder, M.A., White, J.C., Coops, N.C., Hobart, G.W., 2015a. An integrated Landsat time series protocol for change detection and generation of annual gap-free surface reflectance composites. *Remote Sens. Environ.* 158, 220–234. <https://doi.org/10.1016/j.rse.2014.11.005>.
- Hermosilla, T., Wulder, M.A., White, J.C., Coops, N.C., Hobart, G.W., 2015b. Regional detection, characterization, and attribution of annual forest change from 1984 to 2012 using Landsat-derived time-series metrics. *Remote Sens. Environ.* 170, 121–132. <https://doi.org/10.1016/j.rse.2015.09.004>.
- Hermosilla, T., Wulder, M.A., White, J.C., Coops, N.C., Hobart, G.W., Campbell, L.B., 2016. Mass data processing of time series Landsat imagery: pixels to data products for forest monitoring. *Int. J. Digit. Earth* 9, 1035–1054. <https://doi.org/10.1080/17538947.2016.1187673>.
- Li, J., Roy, D.P., 2017. A global analysis of sentinel-2A, sentinel-2B and landsat-8 data revisit intervals and implications for terrestrial monitoring. *Rem. Sens.* 9, 902. <https://doi.org/10.3390/rs9090902>.
- Markham, B.L., Helder, D.L., 2012. Forty-year calibrated record of earth-reflected radiance from Landsat: a review. *Remote Sens. Environ.* 122, 30–40. <https://doi.org/10.1016/j.rse.2011.06.026>.
- Masek, J.G., Skakun, P.S., Ju, J., Claverie, M., Roger, J., Vermote, E., Franch, B., Dungan, J.L., Masek, J., 2018. Harmonized landsat sentinel-2 (HLS) product user's guide (v1.4). Washington D.C., NASA goddard space flight center. https://hls.gsfc.nasa.gov/wp-content/uploads/2019/01/HLS.v1.4.UserGuide_draft_ver3.1.pdf.
- Masek, J.G., Vermote, E.F., Saleous, E.N., Wolfe, R., Hall, F.G., Huemmrich, K.F., Gao, F., Kutler, J., Lim, T.K., 2006. A landsat surface reflectance dataset for north America, 1990–2000. *Geosci. Remote Sens. Lett.* 3, 68–72.
- Matasci, G., Hermosilla, T., Wulder, M.A., White, J.C., Coops, N.C., Hobart, G.W., Bolton, D.K., Tompalski, P., Bader, C.W., 2018a. Three decades of forest structural dynamics over Canada's forested ecosystems using Landsat time-series and lidar plots. *Remote Sens. Environ.* 216, 697–714. <https://doi.org/10.1016/j.rse.2018.07.024>.
- Matasci, G., Hermosilla, T., Wulder, M.A., White, J.C., Coops, N.C., Hobart, G.W., Zald, H.S.J., 2018b. Large-area mapping of Canadian boreal forest cover, height, biomass and other structural attributes using Landsat composites and lidar plots. *Remote Sens. Environ.* 209, 90–106. <https://doi.org/10.1016/j.rse.2017.12.020>.
- Miller, J.D., Knapp, E.E., Key, C.H., Skinner, C.N., Isbell, C.J., Creasy, R.M., Sherlock, J.W., 2009. Calibration and validation of the relative differenced normalized Burn Ratio (RdNBR) to three measures of fire severity in the Sierra Nevada and Klamath Mountains, California, USA. *Remote Sens. Environ.* 113, 645–656.
- Mishra, N., Haque, M., Leigh, L., Aaron, D., Helder, D., Markham, B., 2014. Radiometric cross calibration of landsat 8 operational land imager (OLI) and landsat 7 enhanced thematic mapper Plus (ETM+). *Rem. Sens.* 6, 12619–12638. <https://doi.org/10.3390/rs61212619>.
- Nagol, J.R., Sexton, J.O., Kim, D.-H., Anand, A., Morton, D., Vermote, E., Townshend, J.R., 2015. Bidirectional effects in Landsat reflectance estimates: is there a problem to solve? *ISPRS J. Photogrammetry Remote Sens.* 103, 129–135. <https://doi.org/10.1016/j.isprsjprs.2014.09.006>.
- Pastick, N.J., Wylie, B.K., Wu, Z., 2018. Spatiotemporal analysis of Landsat-8 and Sentinel-2 data to support monitoring of dryland ecosystems. *Rem. Sens.* 10, 791. <https://doi.org/10.3390/rs10050791>.
- Qiu, S., Zhu, Z., Woodcock, C.E., 2020. Cirrus clouds that adversely affect Landsat 8 images: what are they and how to detect them? *Remote Sens. Environ.* 246, 111884. <https://doi.org/10.1016/j.rse.2020.111884>.
- Rengarajan, R., Storey, J.C., Choate, M.J., 2020. Harmonizing the landsat ground reference with the sentinel-2 global reference image using space-based bundle adjustment. *Rem. Sens.* 12, 3132. <https://doi.org/10.3390/rs12193132>.
- Rowe, J.S., 1996. Land classification and ecosystem classification. *Environ. Monit. Assess.* 39, 11–20. <https://doi.org/10.1007/BF00396131>.
- Roy, D.P., Li, J., Zhang, H.K., Yan, L., Huang, H., Li, Z., 2017. Examination of Sentinel-2A multi-spectral instrument (MSI) reflectance anisotropy and the suitability of a general method to normalize MSI reflectance to nadir BRDF adjusted reflectance. *Remote Sens. Environ.* 199, 25–38. <https://doi.org/10.1016/j.rse.2017.06.019>.
- Roy, D.P., Wulder, M.A., Loveland, T.R., W, C.E., Allen, R.G., Anderson, M.C., Helder, D., Irons, J.R., Johnson, D.M., Kennedy, R., Scambos, T.A., Schaaf, C.B., Schott, J.R., Sheng, Y., Vermote, E.F., Belward, A.S., Bindaschadler, R., Cohen, W.B., Gao, F., Hipple, J.D., Hostert, P., Huntington, J., Justice, C.O., Kilic, A., Kovalsky, V., Lee, Z.P., Lymburner, L., Masek, J.G., McCorkel, J., Shuai, Y., Trezza, R., Vogelmann, J., Wynne, R.H., Zhu, Z., 2014. Landsat-8: science and product vision for terrestrial global change research. *Remote Sens. Environ.* 145, 154–172. <https://doi.org/10.1016/j.rse.2014.02.001>.
- Roy, D.P., Zhang, H.K., Ju, J., Gomez-Dans, J.L., Lewis, P.E., Schaaf, C.B., Sun, Q., Li, J., Huang, H., Kovalsky, V., 2016. A general method to normalize Landsat reflectance data to nadir BRDF adjusted reflectance. *Remote Sens. Environ.* 176, 255–271. <https://doi.org/10.1016/j.rse.2016.01.023>.
- Schmidt, G., Jenkerson, C., Masek, J., Vermote, E., Gao, F., 2013. Landsat ecosystem disturbance adaptive processing system (LEDAPS) algorithm description. Reston, VA. <https://doi.org/10.3133/ofr20131057>.
- Shang, R., Zhu, Z., 2019. Harmonizing Landsat 8 and Sentinel-2: a time-series-based reflectance adjustment approach. *Remote Sens. Environ.* 235, 111439. <https://doi.org/10.1016/j.rse.2019.111439>.
- Townshend, J.R., Masek, J.G., Huang, C., Vermote, E.F., Gao, F., Channan, S., Sexton, J.O., Feng, M., Narasimhan, R., Kim, D., Song, K., Song, D., Song, X.-P., Noojipady, P., Tan, B., Hansen, M.C., Li, M., Wolfe, R.E., 2012. Global characterization and monitoring of forest cover using Landsat data: opportunities and challenges. *Int. J. Digit. Earth* 5, 373–397. <https://doi.org/10.1080/17538947.2012.713190>.

- White, J.C., Wulder, M.A., Hobart, G.W., Luther, J.E., Hermosilla, T., Griffiths, P., Coops, N.C., Hall, R.J., Hostert, P., Dyk, A., Guindon, L., 2014. Pixel-based image compositing for large-area dense time series applications and science. *Can. J. Rem. Sens.* 40, 192–212. <https://doi.org/10.1080/07038992.2014.945827>.
- Woodcock, C.E., Allen, R., Anderson, M., Belward, A., Bindschadler, R., Cohen, W., Gao, F., Goward, S.N., Helder, D., Helmer, E., Nemani, R., Oreopoulos, L., Schott, J., Thenkabail, P.S., Vermote, E.F., Vogelmann, J., Wulder, M.A., Wynne, R., 2008. Free access to landsat imagery. *Science* 80 (320). <https://doi.org/10.1126/science.320.5879.1011a>, 1011a–1011a.
- Wulder, M.A., Hilker, T., White, J.C., Coops, N.C., Masek, J.G., Pflugmacher, D., Crevier, Y., 2015. Virtual constellations for global terrestrial monitoring. *Remote Sens. Environ.* 170, 62–76. <https://doi.org/10.1016/j.rse.2015.09.001>.
- Wulder, M.A., Loveland, T.R., Roy, D.P., Crawford, C.J., Masek, J.G., Woodcock, C.E., Allen, R.G., Anderson, M.C., Belward, A.S., Cohen, W.B., Dwyer, J., Erb, A., Gao, F., Griffiths, P., Helder, D., Hermosilla, T., Hipple, J.D., Hostert, P., Hughes, M.J., Huntington, J., Johnson, D.M., Kennedy, R., Kilic, A., Li, Z., Lyburner, L., McCorkel, J., Pahlevan, N., Scambos, T.A., Schaaf, C., Schott, J.R., Sheng, Y., Storey, J., Vermote, E., Vogelmann, J., White, J.C., Wynne, R.H., Zhu, Z., 2019. Current status of Landsat program, science, and applications. *Remote Sens. Environ.* 225, 127–147. <https://doi.org/10.1016/j.rse.2019.02.015>.
- Wulder, M.A., Masek, J.G., Cohen, W.B., Loveland, T.R., Woodcock, C.E., 2012. Opening the archive: how free data has enabled the science and monitoring promise of Landsat. *Remote Sens. Environ.* 122, 2–10. <https://doi.org/10.1016/j.rse.2012.01.010>.
- Wulder, M.A., White, J.C., Loveland, T.R., Woodcock, C.E., Belward, A.S., Cohen, W.B., Fosnight, E.A., Shaw, J., Masek, J.G., Roy, D.P., 2016. The global Landsat archive: status, consolidation, and direction. *Remote Sens. Environ.* 185, 271–283. <https://doi.org/10.1016/j.rse.2015.11.032>.
- Zhang, H.K., Roy, D.P., 2016. Landsat 5 Thematic Mapper reflectance and NDVI 27-year time series inconsistencies due to satellite orbit change. *Remote Sens. Environ.* 186, 217–233. <https://doi.org/10.1016/j.rse.2016.08.022>.
- Zhu, Z., 2017. Change detection using landsat time series: a review of frequencies, preprocessing, algorithms, and applications. *ISPRS J. Photogrammetry Remote Sens.* 130, 370–384. <https://doi.org/10.1016/j.isprsjprs.2017.06.013>.
- Zhu, Z., Woodcock, C.E., 2012. Object-based cloud and cloud shadow detection in Landsat imagery. *Remote Sens. Environ.* 118, 83–94. <https://doi.org/10.1016/j.rse.2011.10.028>.
- Zhu, Z., Wulder, M.A., Roy, D.P., Woodcock, C.E., Hansen, M.C., Radeloff, V.C., Healey, S.P., Schaaf, C., Hostert, P., Strolb, P., Pekel, J.-F., Lyburner, L., Pahlevan, N., Scambos, T.A., 2019. Benefits of the free and open Landsat data policy. *Remote Sens. Environ.* 224, 382–385. <https://doi.org/10.1016/j.rse.2019.02.016>.